

# High-quality-factor viscoelastic nanomechanical resonators from moiré superlattices

Received: 4 July 2024

Accepted: 8 April 2025

Published online: 23 April 2025

 Check for updates

Qin-Yang Zeng<sup>1,7</sup>, Gui-Xin Su<sup>1,7</sup>, Ai-Sheng Song<sup>2,7</sup>, Xin-Yu Mei<sup>1</sup>, Zhi-Yue Xu<sup>2</sup>, Yue Ying<sup>3</sup>, Zhuo-Zhi Zhang<sup>3</sup>, Xiang-Xiang Song<sup>3</sup>, Guang-Wei Deng<sup>4</sup>, Joel Moser<sup>5</sup> , Tian-Bao Ma<sup>2</sup>, Ping-Heng Tan<sup>6</sup>  & Xin Zhang<sup>1,6</sup> 

The moiré superlattice, created by stacking van der Waals layered materials with rotational misalignments, exhibits a multitude of emergent correlated phenomena ranging from superconductivity to Mott insulating states. In addition to exotic electronic states, the intricate networks of incommensurate lattices may give rise to polymer-like viscoelasticity, which combines the properties of both elastic solids and viscous fluids. This phenomenon may enrich the dynamics of nanomechanical resonators, in which viscoelasticity has not played a role thus far. Here, we report on a controllable hysteretic response of the nanomechanical vibrations in twisted bilayer graphene membranes, which we attribute to viscoelasticity. Accompanying this hysteretic response, we measure unusually large mechanical quality factors  $Q$  reaching a remarkably high value of  $\sim 1900$  at room temperature. We interpret the enhancement of  $Q$  as a signature of dissipation dilution, a phenomenon of considerable interest that has recently been harnessed in quantum optomechanical systems. Viscoelasticity features a “lossless” potential that overcomes the corrugation registry and reinforces such a dissipation dilution. Our work introduces the moiré superlattice as a promising system for viscoelasticity engineering through rotating angles and for observing emergent nanoelectromechanical couplings.

Viscoelastic materials display the properties of both viscous liquids and elastic solids<sup>1</sup> known in amorphous polymers<sup>2</sup> and human tissues<sup>3</sup>. In response to a mechanical perturbation, viscoelastic materials exhibit an instantaneous elastic response, followed by a time-dependent mechanical response and energy dissipation. Such time-dependent mechanical behaviours (e.g., stress relaxation and

creep)<sup>4</sup> have led to the discovery of new materials with many useful applications<sup>3,5</sup>, but have so far remained elusive in two-dimensional (2-D) systems. Viscoelastic phenomena may also enrich the dynamics of nanomechanical resonators<sup>6–11</sup>, in which viscoelasticity has not played a role thus far. On the one hand, viscoelasticity may increase dissipation. On the other hand, and counterintuitively, we propose

<sup>1</sup>State Key Laboratory of Semiconductor Physics and Chip Technologies, Institute of Semiconductors, Chinese Academy of Sciences, Beijing 100083, China.

<sup>2</sup>State Key Laboratory of Tribology, Tsinghua University, Beijing, China. <sup>3</sup>CAS Key Laboratory of Quantum Information, University of Science and Technology of China, Hefei Anhui 230026, China. <sup>4</sup>Institute of Fundamental and Frontier Sciences, University of Electronic Science and Technology of China, Chengdu 610054, China. <sup>5</sup>School of Optoelectronic Science and Engineering, Soochow University, Suzhou Jiangsu 215006, China. <sup>6</sup>Center of Materials Science and Optoelectronics Engineering and CAS Center of Excellence in Topological Quantum Computation, University of Chinese Academy of Sciences, Beijing 100049, China. <sup>7</sup>These authors contributed equally: Qin-Yang Zeng, Gui-Xin Su, Ai-Sheng Song. ✉ e-mail: [j.moser@suda.edu.cn](mailto:j.moser@suda.edu.cn); [phtan@semi.ac.cn](mailto:phtan@semi.ac.cn); [zhangxin@semi.ac.cn](mailto:zhangxin@semi.ac.cn)

that it may lower dissipation following a process akin to dissipation dilution<sup>12</sup>.

Stacking 2-D monolayers with rotational misalignment produces a moiré superlattice that can dramatically alter the electronic structure of the system<sup>13–22</sup>. The emergence of an ultra-flat band near the Fermi energy for twisted bilayer graphene (TBG) with a ‘magic angle’ (MA,  $\theta \sim 1.1^\circ$ ) is fundamental to the variety of correlated electronic phases<sup>15–18</sup>. For such a small twist angle, the atomic structural relaxation<sup>23–26</sup> forces the superlattice into an energetically favourable commensurate state by gaining van der Waals energy (pinned state). In contrast, the short moiré period  $\lambda(\theta) = \frac{a}{\sqrt{2-2\cos\theta}}$ , where  $a$  is the lattice parameter of graphene, of TBG with a larger twist angle leads to an incommensurate superlattice with quasi-crystalline orders<sup>27</sup>. Such incommensurate contacting surfaces would slide with negligible friction if they were laterally stiff, a phenomenon called structural superlubricity<sup>28–32</sup>. However, the competition between sliding and pinning in a structurally lubric 2-D interface could make TBGs with an intermediate twist angle retain viscoelastic behaviours, which could offer a basis for developing viscoelastic nanomechanical resonators.

Here, using optomechanical techniques and optical spectroscopy, we measure the vibrations of nanoelectromechanical resonators made of TBG with a moderate twist angle and observe butterfly-shaped hysteresis loops of their resonant frequencies as a function of a gate voltage, a phenomenon we interpret as a viscoelastic behaviour. We study how the shape of these frequency loops evolves as the range and the stepping rate of the gate voltage are changed. Importantly, our observations are repeatable and controllable in all of our devices. Furthermore, by continuously increasing the electrostatic pressure applied to the membrane, we find that the mechanical quality factor  $Q$  is significantly enhanced at room temperature, a counter-intuitive phenomenon we ascribe to dissipation dilution<sup>12</sup> that is reinforced by the reduced intrinsic dissipation. Our work introduces mechanical resonators made from moiré superlattices as promising systems for viscoelasticity engineering through rotating angles, and as dynamic probes to control emergent nanoelectromechanical couplings<sup>33,34</sup>.

## Results

### Large TBG drumhead resonators

The TBG drumhead nanomechanical resonators are prepared by a ‘tear-and-stack’ method using both wet and dry transfer techniques (see Methods). Supplementary Table S1 presents our devices based on their size, their twist angle, and the transfer technique we have used. Figure 1a displays the TBG drums, suspended over cylindrical cavities, that we have investigated. They are labelled as drum 1 (diameter  $D = 6\ \mu\text{m}$ ), drum 2 ( $D = 8\ \mu\text{m}$ ) and drum 3 ( $D = 12\ \mu\text{m}$ ) in Device A. A moderate twist angle  $\theta \sim 12^\circ$  was set during the fabrication and extracted from micro-Raman spectroscopy measurements (see Methods). To drive the flexural vibrations of the drums, a time-dependent gate voltage is applied to the Ti/Au leads as shown in Fig. 1b. The DC component of the resulting force allows us to control the static deflection  $\xi$  and the deflection-induced in-plane stress and strain, while the AC voltage provides a harmonic driving force that actuates the TBG drums. A single laser beam is used to interferometrically measure the mechanical responses of the TBG drums and to simultaneously record the micro-Raman scattering responses of the membrane<sup>35</sup>. All measurements are performed at room temperature under high vacuum (see Methods).

We first estimate  $\theta$  from the moiré superlattice-activated Raman mode. Figure 1c shows the Raman spectrum of the suspended TBG measured at the centre of drum 2 with a 532 nm excitation (see Methods), which shows two main features: the strong G mode and the weak R' mode, arising from the zone-centred (i.e., zero momentum) phonons and the moiré superlattice-activated phonons with momentum  $q(\theta) = \frac{8\pi}{\sqrt{3}a} \sin(\frac{\theta}{2})$  (as shown in the inset to Fig. 1c), respectively. The value of  $\theta$  is extracted from the frequency of the R' mode, which is close to the target value specified in the fabrications. Figure 1d shows the positions of the R' mode and of the G mode as the gate voltage  $V_{\text{dc}}$  decreases from 0 V to  $-9$  V. Surprisingly, both modes are less sensitive to  $V_{\text{dc}}$ , within our experimental accuracy, than the G mode in monolayer graphene (MLG)<sup>35</sup>. Meanwhile, the intensity of the G mode remains almost unchanged for  $V_{\text{dc}}$  down to  $-5$  V before decreasing by

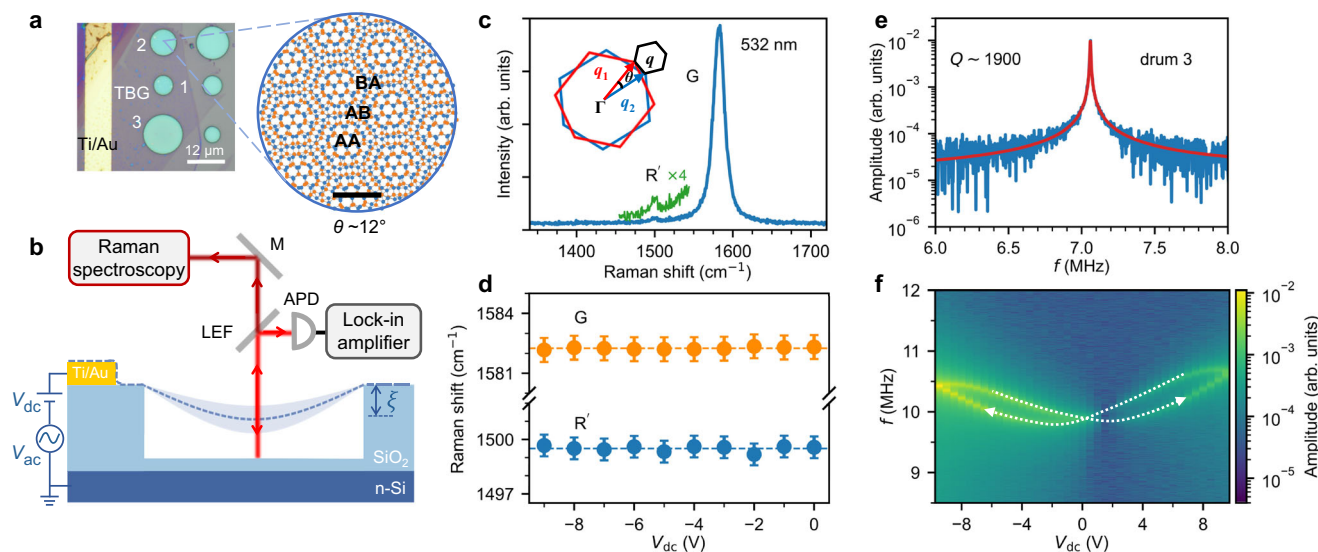


**Fig. 1 | Characterisations of TBG drum and butterfly-shaped hysteresis loop.**

**a** Optical image of Device A with three TBG drums (1, 2, 3) contacted by a Ti/Au lead. The right panel shows the schematics of the moiré pattern formed by a twist angle of  $\theta \sim 12^\circ$ , where alternating AA, AB and BA stacked regions appear (scale bar: 1 nm). **b** Sketch of our experiment combining electrostatic actuation, optical displacement readout, and micro-Raman spectroscopy. The TBG (with its static displacement  $\xi$ ) is represented by the dark blue dashed line; its flexural motion is sketched in light blue. M, LEF, and APD represent a mirror, a long-pass edge filter, and an avalanche photodiode, respectively. **c** Raman spectrum of TBG measured at the

centre of drum 2 ( $D = 8\ \mu\text{m}$ ) by excitation at 532 nm plus the extended spectral region for the R' mode. Inset: a mini-Brillouin zone with a twist angle dependent lattice vector  $q(\theta)$ . **d** The frequencies of the G and the R' modes extracted from Raman spectra measured with  $V_{\text{dc}}$  varying from  $-9$  V to 0 V. The straight dashed line is a guide for the eye. Error bars are extracted from the fits to the Raman spectra. **e** The resonant mechanical response measured in drum 3 ( $D = 12\ \mu\text{m}$ ) at  $V_{\text{dc}} = -10$  V shows a large  $Q$  of  $\sim 1900$  at room temperature. **f** Mechanical frequency responses measured with  $V_{\text{dc}}$  undergoing the forward-then-backward sweep sequence (indicated by arrows), forming a butterfly-shaped hysteresis loop.

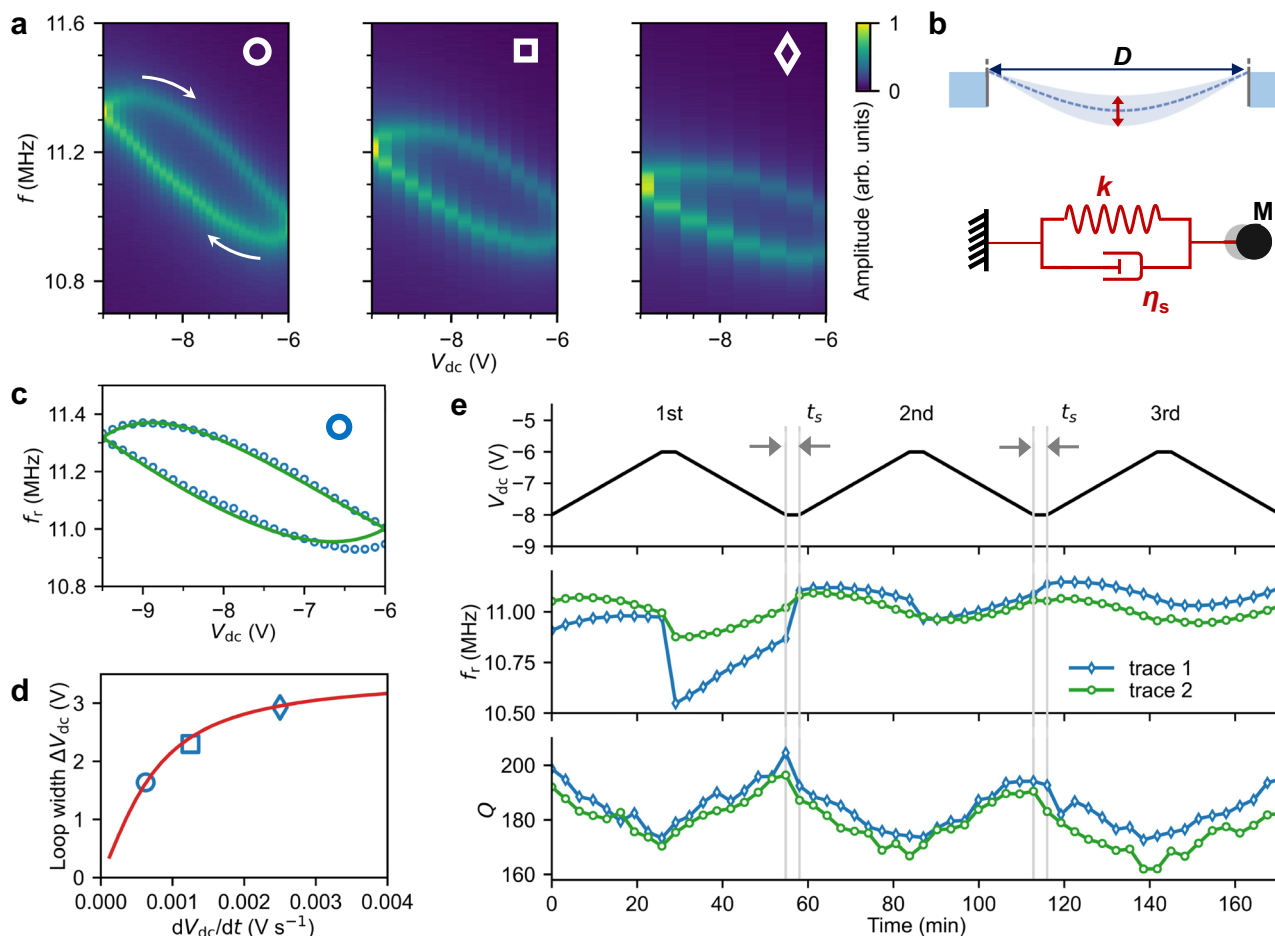


**Fig. 2 | Rate and time dependent hysteresis loops and gate tuning of the quality factors  $Q$ .** **a** Resonant frequency loops at different step rates,  $dV_{dc}/dt$ .  $\circ$ ,  $\square$ ,  $\diamond$  correspond to a slow, medium, and fast step rate, respectively. The arrows indicate the direction of the sweep. **b** Schematic of the flexural drum vibration (top panel) and the reduced viscoelastic model (bottom panel). The membrane flexural motion is modelled by a mass ( $M$ ) connected to a spring ( $k$ ) and a dashpot ( $\eta_s$ ) in parallel (Kelvin-Voigt model) to include the effects of viscoelasticity.  $D$  is the diameter of

the drum. **c** Experimental and fitted ( $\epsilon_0 = 2.67 \times 10^{-4}$  and  $\eta_s = 10.5 \times 10^{15}$  Pa s) resonant frequency loop under the slow stepping rate ( $\circ$ ). **d** Experimental and calculated  $\Delta V_{dc}$  as a function of  $dV_{dc}/dt$ . **e** Evolution of  $f_r$  and  $Q$  upon repeating the forward-then-backward step sweep of  $V_{dc}$  in three consecutive rounds (1st, 2nd, 3rd) for two traces (trace 1 and trace 2) corresponding to different initialisations.  $t_s$  is the time interval (only denoted between two different rounds) when the step direction is reversed.

~ 10% at  $V_{dc} = -9$  V (see Fig. S1c and Methods). These observations indicate that the  $V_{dc}$ -induced tensile strain is negligible compared to the initial built-in strain ( $\epsilon_0$ ), which means that our TBG drums are under high tensile stress.

### Large $Q$ at room temperature

Figure 1e shows the mechanical response of drum 3 ( $D = 12 \mu\text{m}$ ) at  $V_{dc} = -10$  V. The resonant frequency  $f_r$  and corresponding  $Q$  are extracted by fitting a linear harmonic resonator model to the measured response (see Methods). The largest  $Q$  we measure reaches ~1900 at room temperature, more than one order of magnitude higher than  $Q$  in graphene resonators at room temperature<sup>9</sup>. Note that such large  $Q$  appears at the gate voltage far from the near-zero DC bias, in contrast to graphene resonators<sup>35</sup>. We observe that resonances with unusually large  $Q$  exhibit a butterfly-shaped hysteresis loop as the gate voltage is cycled.

### Butterfly-shaped hysteresis loop

To measure the hysteretic nanomechanical responses, we increase and decrease the gate voltage in cycles. Figure 1f shows the amplitude response as a function of drive frequency and  $V_{dc}$  under a forward-then-backward sweep between  $V_{dc} = \pm 9.5$  V, forming a butterfly-shaped hysteresis loop that crosses at  $V_{dc} = 0$  V (white-dashed arrows

in Fig. 1f). Within the butterfly-shaped hysteresis loop,  $f_r$  increases by only ~5%, which is far less than the typical value of ~50% in the low-tensioned MLG drum<sup>35</sup>. Note that all of the mechanical data in this study are from drum 2 in Device A unless otherwise stated. The butterfly-shaped hysteresis loop also shrinks as the sweep range decreases (Fig. S5a). We find that such viscoelastic responses can be controllably obtained by specifying  $\theta$  close to  $15^\circ$  in our TBG drums, whereas the TBG with  $\theta = 0^\circ$  does not show a butterfly-shaped hysteresis loop. Supplementary Section S3 provides the statistics on the hysteresis loops of our TBG drums with increasing  $\theta$ . It suggests that the viscoelasticity in TBG drums is angle-dependent, as we discuss below.

### Viscoelastic behaviours

To study the dependence of the shape of the frequency loop on the step rate  $dV_{dc}/dt$ , in Fig. 2a we show the hysteresis loops measured at three different values of  $dV_{dc}/dt$ . They have been recorded in a backward-then-forward sequence with a step size of 0.25 V. Remarkably, the maximal  $f_r$  reached by the loop is revealed with the slow step rate. Furthermore, the width of the hysteresis loop,  $\Delta V_{dc}$ , defined by the largest  $V_{dc}$  shift between the forward and backward traces, shows a non-linear monotonic increase with increasing  $dV_{dc}/dt$ , as shown by the experimental data in Fig. 2d.

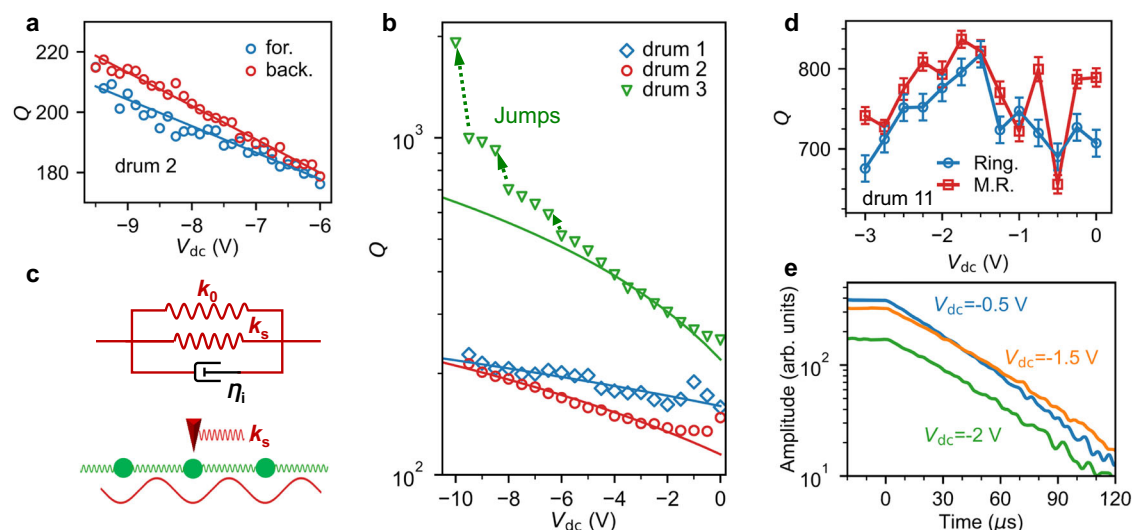


**Fig. 3 | Viscoelastic dissipation dilution.** **a** Quality factors  $Q$  corresponding to Fig. 2c for both forward and backward sweeps. **b**  $Q$  extracted from the mechanical response spectra and as a function of  $V_{dc}$  for drum 1 ( $D = 6 \mu\text{m}$ ), drum 2 ( $D = 8 \mu\text{m}$ ) and drum 3 ( $D = 12 \mu\text{m}$ ), respectively. The dashed arrows denote the  $Q$  jumps revealed in drum 3. The solid lines in (**a**, **b**) are linear fits to the experimental data (see Supplementary section S2.2). **c** Top panel: the extended Kelvin-Voigt model, i.e., the intrinsic friction dashpot  $\eta_i$  is added in parallel to the model that has been introduced in Fig. 2b, but here  $\eta_s$  is explicitly replaced by a “lossless” viscoelastic

spring  $k_s$ . Bottom panel: a cartoon of the Prandtl-Tomlinson model, where the tip slides on top of a one-dimensional chain of springs, which moves on top of a fixed potential. **d** The  $V_{dc}$ -dependent  $Q$  extracted from the ring-down measurements (Ring.) and fitting of the mechanical responses (M.R.) in drum 11 ( $D = 12 \mu\text{m}$ ) of Device E. Error bars in the traces of Ring. and M.R. are extracted from the fits of energy decay and mechanical responses, respectively. Note that the ringdown trace has been shifted up by 50 for direct comparison (see Methods). **e** Energy decay traces (in log scale) at different  $V_{dc}$  in drum 11 ( $D = 12 \mu\text{m}$ ) of Device E (see Methods).

Below we consider various mechanisms that may explain our observations. We rule out contamination as the origin of the viscoelastic behaviour by reproducing the hysteresis loop on optimally clean TBG drums fabricated by the all-dry transfer method (see Supplementary section S1.4 for surface characterization by atomic force microscopy). Euler instabilities<sup>36</sup> and mechanically conservative nonlinearities<sup>36</sup>, which would also give rise to hysteresis frequency loops, can be safely ruled out. Nonlinearities can be disregarded because the shape of our frequency loops does not depend on the strength of the driving force (Fig. S9). Sliding motion at the clamping points can also be excluded because such a sliding produces a plateau for  $f_r$  near the switching points<sup>37</sup>.

Alternatively, a process that may account for our observations is a viscoelastic one. We model the TBG drums as a spring and a dashpot connected in parallel (Fig. 2b), known as the Kelvin-Voigt model (KVM), to include the effects of viscoelasticity<sup>1</sup>. The constitutive relation is expressed as a first-order linear differential equation,  $\sigma = E(\epsilon + \tau_\sigma \frac{d\epsilon}{dt})$ , where  $\sigma$  is stress,  $\epsilon$  is strain,  $E$  is Young's modulus,  $\tau_\sigma = \eta/E$  is the relaxation time, with  $\eta$  the viscosity of the material. Based on this constitutive equation, the resonant frequency of TBG drums is expressed as (see Methods):

$$f_r = \frac{1}{2\pi} \sqrt{\frac{E}{4m_{\text{eff}}D^2}(k_0 + k_s)} \quad (1)$$

with the normal term  $k_0 = 2\epsilon_0 + \frac{3}{2}z^2$ , the viscoelastic term  $k_s = \frac{3}{2}\tau_\sigma z \frac{dz}{dt}$ , where  $z = \xi/D$  is the dimensionless deflection at the centre of the drum,  $\epsilon_0$  is the built-in strain,  $\tau_\sigma = \eta_s/E$  with  $\eta_s$  the viscosity of the dashpot, and  $m_{\text{eff}}$  is the effective mass of the vibrational mode. The dynamical equation of motion for  $z$  can be constructed from the force equilibrium relation (see Methods). The parameters obtained by numerically solving the dynamical equation are plugged into Eq. (1) to calculate  $f_r$ . Using these experimental parameters, the KVM reproduces the shape of the frequency loops well, as shown in Fig. 2c for a slow step rate (see Supplementary section S2.2 for the fits to butterfly-shaped loops and the stepping-dependent butterfly-shaped loops). The model also reproduces the relationship between  $\Delta V_{dc}$  and  $dV_{dc}/dt$

(Fig. 2d). The implications of the non-linear relationship revealed in Fig. 2d are twofold: first,  $\Delta V_{dc}$  will decrease to zero for an extremely slow rate, namely without any hysteresis loop; second,  $\Delta V_{dc}$  will saturate for a fast rate, corresponding to the case where the dynamic system can not follow the external stimuli. Therefore, the time dependence of  $f_r$  is slow on the scale of the ring-down time and on the scale of the vibrational period.

To gain an intuitive understanding of the behaviour of TBG drums as the gate voltage is cycled, we estimate the damping force,  $F_d = S \cdot \eta_s \frac{dz}{dt} \approx 1.859 \times 10^{-4} \text{ N}$ , with  $S$  the surface area of the drum and viscous energy losses  $E_v = S \cdot \int \eta_s \frac{dz}{dt} d\epsilon \approx 1.41 \times 10^{-13} \text{ J}$ , based on the frequency loop in Fig. 2c which we fit with two parameters, namely  $\epsilon_0 = 2.67 \times 10^{-4}$  and  $\eta_s = 10.5 \times 10^{15} \text{ Pa s}$ , yielding  $\tau_\sigma \approx 10^4 \text{ s}$ . Our damping force corresponds to a shear stress  $\gamma = F_d/S \approx 3.7 \text{ MPa}$ , which is larger than in bilayer graphene<sup>38</sup>, but comparable to that in twisted  $\text{MoS}_2$ <sup>39</sup>. The proportions of  $k_0$  and  $k_s$  corresponding to Fig. 1e and Fig. 2c are provided in Fig. S6b and Fig. S7c, respectively. We find that the increase in  $f_r$  within the frequency loop can be fully accounted for by the viscoelastic spring constant  $k_s$ . For drum 4 in Device B where  $V_{dc}$  is cycled between  $-5 \text{ V}$  and  $-1 \text{ V}$ , we obtain  $\epsilon_0 = 3.82 \times 10^{-4}$ ,  $\eta_s = 8.9 \times 10^{15} \text{ Pa s}$ ,  $\tau_\sigma \approx 10^4 \text{ s}$ ,  $F_d \approx 2.867 \times 10^{-4} \text{ N}$ ,  $E_v = 6.1 \times 10^{-14} \text{ J}$ , and  $\gamma \approx 2.5 \text{ MPa}$ .

We further test the dynamic nature of the system by repeating the backward-then-forward sweeps in three consecutive rounds, as shown in Fig. 2e. Two traces are recorded, corresponding to different initial  $f_r$ . A slow convergence to a steady state, where a perfect loop, i.e., with no gaps or crossings at the switching points, is observed in the third round. Trace 2 shows a much smoother path as its initial  $f_r$  closed to the steady state.

Furthermore, within a resonant frequency loop, we find that  $Q$  follows  $f_r$ , both increasing and decreasing concomitantly. The tunability of  $Q$  shows an approximately linear increase as decreasing gate voltage (Fig. 2e). Such enhancements of  $Q$  are expected to depend on the gate voltage stepping rate (see Fig. S11a) via  $k_s$  as discussed above. These observations are in stark contrast to the conventional phenomena for 2-D nanoelectromechanical resonators, where the  $Q$  decreases rapidly with increasing electrostatic pressure, which is still a subject of debate<sup>35</sup>.

## Viscoelastic dissipation dilution

To explore the mechanism of energy dissipation related to high-frequency mechanical vibrations (tens of MHz), in Fig. 3a we show  $Q$  extracted from the frequency loop corresponding to Fig. 2c, where the linear increments with slightly different slopes are revealed for forward and backward sweeps with a step size of 0.25 V. The different increments in  $Q$  under other step rates are given in Fig. S11a. Figure 3b summarises  $Q$  as a function of  $V_{dc}$  for three drums in Device A. The large drum tends to have a large  $Q$ , which is consistent with many reports in the literature<sup>40</sup>. There are also a few jumps in  $Q$ , as shown in Fig. 3b for drum 3 under a large gate voltage sweep. Such an observation may suggest the existence of further stick-slip actions beyond the atomic scale<sup>41</sup>.

Firstly, we use our estimates of  $\eta_s$  and  $\epsilon_0$  to estimate the contribution of dissipation dilution in our measurements. The phenomenon of dissipation dilution refers to the reduction in energy dissipation from the contribution of a lossless potential that stores part of the elastic energy of mechanical resonators. The lossless potential may originate from e.g., a geometrical nonlinear deformation<sup>12</sup>. Such dissipation dilution could not explain our observations, since the small elastic energy increments are fully accounted for by the viscoelastic term  $k_s$  in Eq. (1). However, due to a long viscoelastic relaxation time ( $\tau_{os} \approx 10^4$  s for drum 2) compared to the vibrational period  $\approx 10^{-5}$  s, such a term can play a similar role as that of a nonlinear deformation to store elastic energy and contribute a “lossless” spring constant  $k_s$  within the period of the oscillator. In order to provide an intuitive picture, we propose an extended KVM (Fig. 3c, top panel), where the intrinsic dissipation is modelled by a new dashpot ( $\eta_i$ ) in parallel to the spring ( $k_0$ ) and viscoelastic dashpot ( $\eta_s$ ) that have been introduced in Fig. 2b, but here  $\eta_s$  has been replaced by  $k_s$ . The intrinsic  $Q$  can be defined by the material loss tangent,  $Q_{int} = 1/\tan(\phi)$ , where  $\phi$  is the phase lag between stress and strain.  $Q$  is characterised by  $Q = D_Q \times Q_{int}$ , where  $D_Q = (1 + k_s/k_0)$  is called the dilution coefficient. Based on the outputs from KVM (see Fig. S7),  $D_Q \approx 1.06$  is found for  $V_{dc} = -9.5$  V as compared to  $V_{dc} = -6$  V, which is less than the experimental  $D_Q \approx 1.20$  (forward) and  $D_Q \approx 1.22$  (backward), as shown in Fig. 3a.

We further estimate the impacts of  $k_s$  on intrinsic damping rate  $\Gamma = f/Q_{int}$ , which is not included in the conventional model of dissipation dilution<sup>12</sup>. The extracted  $\Gamma$  corresponding to Fig. 3b is shown in Fig. S10a. Notably, three drums in Device A follow a similar slope of  $\sim 3$  kHz V<sup>-1</sup>. Intrinsic damping arises from the atomic-scale stick-slip behaviour that gives rise to friction. It is commonly interpreted by the Prandtl-Tomlinson model, where a particle is pulled by a linear spring of stiffness  $k_d$  to slide on a periodic energy landscape (Fig. 3c, bottom panel). The stick-slip action only occurs if the corrugation registration energy is large enough, i.e.,  $2E_0\pi^2/k_d b^2 > 1$ , where  $E_0$  and  $b$  are the amplitude and period of the energy corrugation<sup>42</sup>. Otherwise, the stick-slip behaviour would undergo the transition to continuous motion without dissipation, thus reducing  $\Gamma$ . The viscoelastic stiffness  $k_s$  creates a lateral, time-dependent heterostrain that makes the atom slide on a lattice (Fig. 3c, bottom panel), and as such can be considered as a driving  $k_d$ . The sliding resistance can be reduced or even eliminated by increasing  $k_s$  by  $V_{dc}$ , reinforcing the effect of dissipation dilution.

Our mechanism of reinforced viscoelastic dissipation dilution is markedly different from the electrical tuning of  $Q$  in nanotubes<sup>13,44</sup>. It is also different from the electrical tuning of  $Q$  in graphene due to Ohmic dissipation, where  $Q$  decreases as  $|V_{dc}|$  increases<sup>45</sup>. Because our measurements do not involve charge transport through the resonator, we believe that the phenomena we observe have a purely mechanical origin. Remarkably, a transition from the purely mechanical region with enhanced  $Q$  to the usual electrostatic region with decreased  $Q$  as increasing  $|V_{dc}|$  is revealed for with  $\theta \sim 4^\circ$  (Fig. 3d), with  $\theta \sim 10$ .  $5^\circ$  (Fig. S16d) and another drum of  $\theta \sim 12^\circ$  (Device G) with a small built-in strain introduced by annealing (Fig. S8i). In fact, we can separate the dissipation as  $1/Q = 1/Q_{normal} + 1/Q_{viscoelastic}$ . Thus, if the normal term competes with the viscoelastic one, either by reducing  $\epsilon_0$  as in Device G

or by reducing viscosity in the case of a small twist angle (Device E), the electrostatic region with decreased  $Q$  returns.

To obtain the direct information on the dissipation dynamics, we further perform the ring-down measurements (see Methods) in drum 11 of Device E. The vibrational amplitude at resonant frequency decays exponentially in time as  $\propto e^{-t/(2\tau)}$  upon stopping the drive, with  $\tau$  the decay time constant, which gives  $Q = 2\pi f_r \tau$ . The energy decay traces (in log scale) corresponding to different  $V_{dc}$  are shown in Fig. 3e.  $Q$  obtained from the ring-down measurements is identical to the trajectory extracted by fitting of the mechanical responses (Fig. 3d). Further controlled ring-down measurements using gate voltage pulses or tiny ramps to capture the discrete  $Q$  jumps (as shown in Fig. 3b) are needed to elucidate the underlying mechanism.

## Discussion

Finally, we discuss the origin of the viscoelasticity revealed in our TBG drums. For small  $\theta$ , e.g., MA, the incommensurate lattice with neighbouring AA, AB, and BA stacking domains will spontaneously transform into a commensurate one by gaining interlayer interaction energy. Thus, they have to overcome a relatively large  $E_0$  in order to slide, similarly to commensurate AA- and AB-stacked bilayer graphene. By contrast, an incommensurate lattice can overcome  $E_0$  and easily enable interfacial sliding, up to the extreme of superlubricity. Thus, two MLG sheets in an incommensurate TBG with a twist angle between two extremes tend to behave individually, similarly to the molecular chains in a polymer.

Figure 4a shows the prototypical nanofriction setup for Molecular dynamics (MD) simulations. Figure 4b shows that the predicted coefficient of friction (COF) from MD simulations (see Methods) decreases with increasing  $\theta$  between  $10^\circ$  and  $14^\circ$ . Indeed, the butterfly-shaped hysteresis loops are more easily revealed on TBG with  $\theta \sim 13$ .  $5^\circ$  (Fig. S8j),  $\theta \sim 12^\circ$  (Fig. S8f-h, i) than  $\theta \sim 4^\circ$  (Fig. S8c-e),  $\theta \sim 1$ .  $1^\circ$  (Fig. S8k),  $\theta \sim 0$ .  $4^\circ$  (Fig. S8b) in our studies. In particular, TBG with very small  $\theta \sim 0$ .  $4^\circ$  (Fig. S8b) and the bilayer graphene (Fig. S8a) do not show any hysteresis loops, instead, they show a capacitive softening of their spring constant as  $|V_{dc}|$  is increased<sup>46</sup>. To obtain an intuitive picture, we further simulate the COF of TBG under heterostrain. The COF shows dual-scale oscillations due to both atomic and moiré-scale dual-periodic friction force as expected. More importantly, our simulation indicates that COF follows a linear decreasing trend with the applied heterostrain, which could explain the revealed linear trend in damping rates (Fig. S10a).

The observed transition from capacitive softening (bilayer graphene drum) to butterfly-shaped hysteresis loops (softening-to-butterfly transition) with increasing  $\theta$  suggests that viscoelasticity in TBG is angle-dependent (see Fig. S8). We extend our KVM to include capacitive softening effects (see Methods) and reproduce this softening-to-butterfly transition as the strength of viscoelasticity ( $\eta_s$ ) increases, as shown in Fig. 5. It directly introduces the twist angle as an effective knob that tunes viscoelasticity in moiré superlattices.

In conclusion, we report on viscoelasticity in TBGs with different misalignments. The viscoelasticity originates from sliding between two incommensurate layers. The resonant frequency loops show a strong dependence on gate voltage and are well reproduced by our viscoelastic model. The lateral, time-dependent stiffness resulting from the viscoelasticity contributes a “lossless” potential for mechanical vibrations and dramatically reduces the intrinsic damping rates, providing a remarkably high value of  $Q \sim 1900$  at room temperature. The revealed viscoelasticity originates from interfacial sliding enabled by both an incommensurate lattice and a strong built-in strain.

Our work introduces twisted 2-D systems with rotational freedom as a platform for viscoelasticity engineering in ultra-thin membranes. The remarkably high  $Q$  make TBGs promising for the study of nanoscale friction and emergent nanoelectromechanical and spin-mechanical couplings. These are regularly achieved, by further

increasing the drum size to increase  $Q$  and at cryogenic temperatures, or by tensioning twisted membranes based on microelectromechanical systems<sup>47</sup>. The embedded nature of nanomechanical resonators and their extreme sensitivity to the environments enable the study of correlated phase transition, atomic or lattice dynamics and thermodynamics. Going one step further, with the emergence of 2-D systems with robust magnetic order and topological phases<sup>48</sup>, we foresee new opportunities to explore and exploit viscoelastic properties, for example, to construct new generation of dynamically slippable microsystems<sup>49</sup> and reconfigurable interfaces<sup>50</sup>.

## Methods

### Device fabrication

The TBG drumhead nanoelectromechanical resonators were prepared in two sequential parts, including the TBG flake preparation and deterministic transfer onto pre-patterned holes. A “tear-and-stack” method was used to obtain large TBG flakes: first, large monolayer graphene flakes were randomly deposited on 285 nm-SiO<sub>2</sub>/Si substrates, using a thermally assisted mechanical exfoliation scheme as described in ref. 51. The thickness of the graphene was confirmed by micro-Raman spectroscopy. The target flake is then rapidly cut into

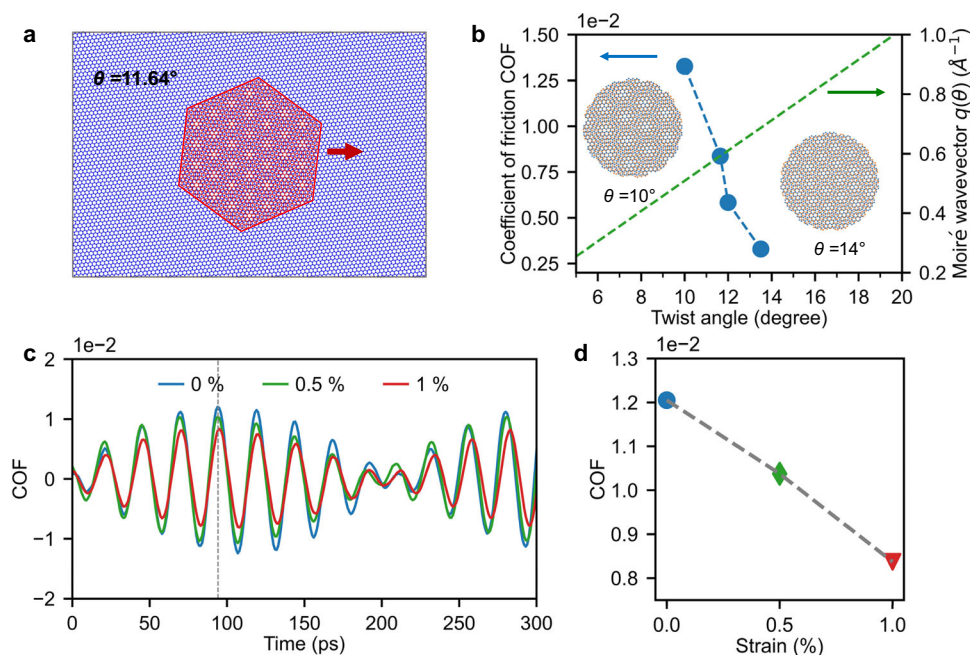


**Fig. 4 | Reduced friction by lateral heterostrain.** **a** Top view of prototypical nanofriction setup for Molecular dynamics (MD) simulations: a hexagonal AB-stacked bilayer graphene flake is sliding (as indicated by the red arrow) on a rectangular AB-stacked bilayer graphene substrate. **b** The coefficient of friction (COF) in the TBGs with 1% heterostrain as a function of twist angle, which follows a decreasing trend. The right axis shows the moiré wavevector  $q(\theta)$ . Inset: the moiré

patterns formed by the twist angles of  $10^\circ$  and  $14^\circ$ . **c** COF as a function of time for the cases with no heterostrain 0%, 0.5% and 1% heterostrain cases under a normal force of 2 GPa for the TBG with  $\theta = 11.64^\circ$  (see Methods), showing the dual-scale oscillations. The dark-dashed line indicates the line cut for the extraction of the COF in (d). **d** Reduced COF with increasing heterostrain level, which follows a linear decreasing trend.

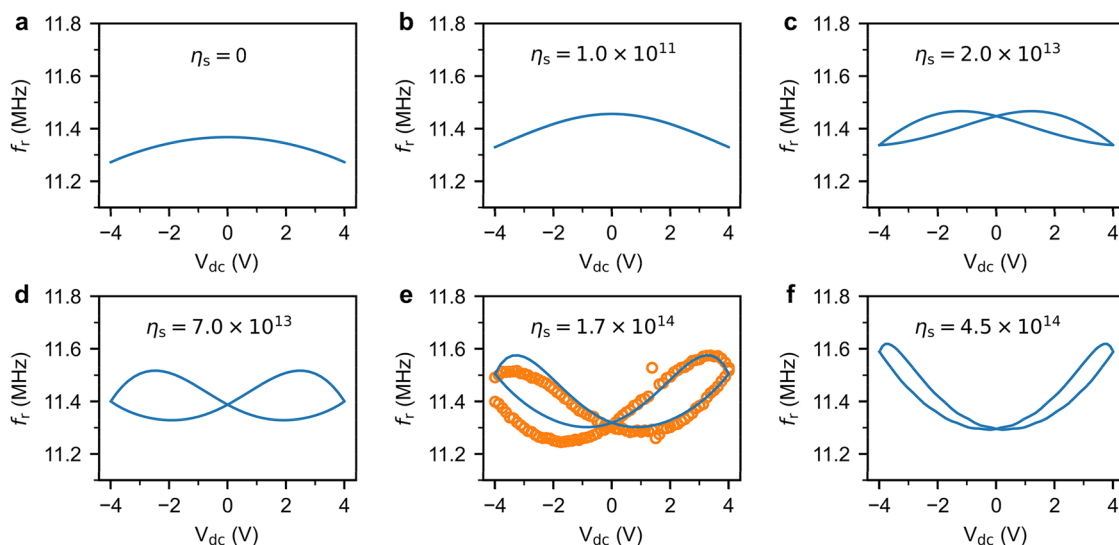


**Fig. 5 | Softening-to-butterfly transition.** **a–f** The resonant frequency tuning calculated by KVM with capacitive softening (see Methods) as  $\eta_s$  increases from 0 to  $4.5 \times 10^{14}$  Pa s, which shows the transition from the capacitive softening to the

butterfly-shaped hysteresis loop. The experimental butterfly loop in (e) is measured in drum 8 ( $D = 8 \mu\text{m}$ ) of Device D with  $\theta = 12^\circ$ .

two halves of similar size using a diamond tip, of which one half is picked up either by a capillary force assisted wet transfer techniques<sup>52,53</sup> or by a van der Waals force assisted dry transfer techniques. The wet transfer method: in practice, a polydimethylsiloxane (PDMS) stamp is first applied to the substrate with the contact boundary moving smoothly towards the cutting scratch, eventually covering half of the graphene flake. Care should be taken not to completely cover the scratch. A water droplet is injected from the side entrance of the substrate, spreads out and makes contact between the PDMS and another half graphene supported by capillary force, and finally dries naturally, while attaching the graphene flake to the PDMS stamp. This lifted graphene flake (PDMS/graphene) is then pressed onto the one left on the substrate at a specified angle of rotation by a high-precision rotary stage, which removes the attached graphene and deposits a TBG flake on the substrate. In the second part, another PDMS stamp picks up the stacked flake and deposits it onto a pre-patterned substrate that has been treated with oxygen plasma to increase adhesion. The dry transfer method: one sizeable h-BN flake with a well-defined window is used to successively pick up two halves of the graphene flake and then deposits it onto a pre-patterned substrate (Fig. S4d). The pattern is created by optical lithography followed by reactive ion etching and consists of hole arrays (4, 6, 8, 10, and 12  $\mu\text{m}$  in diameter and  $250 \pm 5$  nm in depth) completely separated or connected by 1  $\mu\text{m}$ -wide ventilation channels (Supplementary Section S1.1). Ti(5 nm)/Au(45 nm) contacts close to hole arrays are evaporated by electron beam. We have carefully optimised the entire fabrication process to minimise ripping and crumpling effects, as evidenced by the moderate  $Q$  found on TBG drums with different twist angles and good surface quality measured by atomic force microscopy (Fig. S4).

### Optomechanical measurements

Electrically connected TBG drums are mounted in a vacuum chamber ( $6 \times 10^{-6}$  mbar). The drum arrays are capacitively driven using the heavily n-type doped Si wafer as a backgate, and a time-dependent gate bias  $V_g(t) = V_{dc} + V_{ac} \cos \Omega t$  is applied as described in the main text. The electrostatic force applied is given by  $F_{el} = \epsilon_v \pi D^2 V_g^2(t) / 8d^2(\xi)$ , where  $D$  is the diameter of the drum,  $\epsilon_v$  is the vacuum dielectric constant,  $d(\xi) = (d_{vac} - \xi) + d_{SiO_2} / \epsilon_{SiO_2}$  is the effective distance between the TBG drum and the Si substrate, where  $\xi$  is the static displacement at the centre of the drum,  $d_{vac}$  is the distance between the TBG drum and  $SiO_2$  in the absence of any gate bias,  $d_{SiO_2}$  is the thickness of the residual  $SiO_2$  layer. This force includes a static component proportional to  $V_{dc}^2$ , which determines the value of  $\xi$ , and a harmonic driving force proportional to  $V_{dc} V_{ac} \cos(\Omega t)$ . Note that since  $V_{ac} \ll |V_{dc}|$ , we can safely neglect the force  $\propto V_{ac}^2 (1 + \cos(2\Omega t))$  throughout our analysis. At the same time, we always use a low drive power to avoid any vibration nonlinearities (Supplementary Section S6). A 632.8 nm He-Ne continuous wave laser with a power of  $\sim 150$   $\mu\text{W}$  is focused onto a  $\sim 1.2$   $\mu\text{m}$ -diameter spot and is used for optomechanical measurements. The opto-thermal effects on  $Q$  are safely excluded by measuring at different laser powers (Supplementary Section S7). Unless otherwise stated, measurements are made at the centre of the drum. The beam reflected from the cavity of Si/ $SiO_2$ /vacuum/TBG layered geometry is detected by an avalanche photodiode. In the driven regime, the mechanical amplitude at  $f = \Omega/2\pi$  is readout using a lock-in amplifier. The values of  $f_r$  and  $Q$  are extracted by fitting the mechanical response with linear response theory of a driven harmonic oscillator. The amplitude ( $z_0$ ) of mechanical displacement  $z = z_0 e^{2\pi i f t}$  is expressed as<sup>35</sup>

$$|z_0|^2 = \frac{1}{16\pi^4} \frac{(\tilde{F}_{el}/m_{eff})^2}{(f_r^2 - f^2)^2 + (f_r f/Q)^2} \quad (2)$$

where  $\tilde{F}_{el}$  is the effective applied electrostatic force,  $m_{eff}$  is the effective mass density which takes into account the shape of the vibrational mode<sup>54</sup>. Note that the formal data collection on the TBG drums without any ventilation channels was performed after waiting more than five days and continuing for two or three weeks.

### Sweeping measurements

An automatic programme based on Python is launched to perform the forward and backward sweeps, implemented on a lock-in amplifier. The forward-then-backward, backward-then-forward, and multiple sweep functions are constructed by specific scripts. By default, the program creates a time interval when the sweep direction is changed. The specific step size is defined by the program. To calculate the step rates, we divide the total run time by the specified step size, which is further cross-checked by the time it takes to run a frequency sweep process on the lock-in amplifier with the same configurations. Note that we do not set up the initial state by program, instead, we manually change the applied  $V_{dc}$  with a small step size (typically, of 0.1 V), to avoiding collapsing TBG drums (especially those with  $D = 12$   $\mu\text{m}$ , see Supplementary Section S1.2) and to allow the dynamic system to reach a steady state before loading any sweep programs.

### Optical micro-spectroscopy

Raman spectra are recorded on our custom-designed SmartRaman system, which uses a 550 mm monochromator equipped with an 1800 grooves/mm grating, coupled to a cooled CCD array. The Raman signals excited at 632.8 nm or 532 nm are filtered using ultra-steep long-pass edge filters. The laser power is kept below  $\sim 0.4$  mW to avoid any heating of the sample. The Raman  $R'$  mode and G mode spectra are fitted with a Lorentzian function. The value of  $\theta$  can be estimated directly from the frequency of the  $R'$  mode whose involved phonon momentum  $q(\theta) = \frac{8\pi}{\sqrt{3}a} \sin(\frac{\theta}{2})$ , where  $a$  is the lattice parameter of graphene. Raman enhancements due to the van Hove singularities in the conduction and valence bands occur at the critical twist angle  $\theta_C = \frac{3aE_F}{\hbar v_F 4\pi}$ , where  $v_F$  is the Fermi velocity in monolayer graphene,  $E_F$  excitation energy<sup>55</sup>. For an excitation of 532 nm (632.8 nm),  $\theta_C \sim 12.3^\circ$  ( $10.3^\circ$ ). So we use 632.8 nm excitation for spectra measurements on TBGs with  $\theta \sim 10^\circ$ , and 532 nm for TBGs with  $\theta \sim 12^\circ$  and  $\theta \sim 13.5^\circ$ . In addition, the Raman intensity of the G mode is designed to increase monotonically as the membrane moves towards the bottom of the holes (see Supplementary Section S1.1). Thus, the detected  $\sim 10\%$  decrease in Raman G mode intensity can be attributed to the small changes in twist angle which keeps away from  $\theta_C$ . In fact, an increasing trend in Raman G mode intensity was observed for TBG with  $\theta \sim 10.5^\circ$  (Fig. S16b) and the as-annealed TBG with  $\theta \sim 12^\circ$  (Fig. S3c).

### Ring-down measurements

The ring-down measurements were performed with a dual-channel (CH1 and CH2) arbitrary waveform generator (AWG). A burst signal from the external triggered burst mode in CH1 with the carrier frequency same to the resonant frequency is used to drive the mechanical resonator. CH2 is used to provide a square wave (typically 1 kHz with a 50% duty cycle) as the external trigger for both CH1 and an oscilloscope (with a sampling rate of 5 GSa  $s^{-1}$ ). We also used a low-noise amplifier (voltage gain of 125, noise figure of 1 dB) to amplify the output voltage of the avalanche photodiode. We first run a backward voltage sweep starting at  $V_{dc} = 0$  V, with a typical step size of  $\sim 0.25$  V, from which  $Q$  is extracted by fitting the mechanical responses. The same  $V_{dc}$  history is required for comparison with the ring-down measurement (Fig. 3e). Therefore, we gradually recovered to  $V_{dc} = 0$  V and waited an hour or two before performing the ring-down measurement. In the meantime, we keep the same time interval in the ring-down measurement as in the gate voltage sweeps. The time traces recorded by the oscilloscope are further field averaged 2048 times. To extract the envelope of the averaged traces, a bandpass filter (with a

bandwidth of 400 kHz) is applied, followed by a standard low-pass filtering of the vibration power. The vibrational amplitude decays exponentially in time as  $\propto e^{-t/(2\tau)}$ , where  $\tau$  is the decay time constant, yielding  $Q = 2\pi f_r \tau$ . Note that we use vibrational amplitude field averaging rather than offline post-power averaging<sup>56</sup>, which may account for the offset shown in Fig. 3d.

### Viscoelasticity modelling

The drumhead resonator is modelled as a pre-tensioned, suspended membrane resonator with fixed boundaries and a parabolic mode shape. The strain at membrane deflection is therefore given by  $\epsilon = \epsilon_0 + \frac{z^2}{4}$ , where  $z = \xi/D$  is the dimensionless deflection at the centre of the drum. The corresponding stress is related to strain by a Kelvin-Voigt constitutive relation,  $\sigma = E\epsilon + \eta \frac{d\epsilon}{dt}$ , where  $E$  is Young's modulus and  $\eta$  is viscosity coefficient. The total mechanical energy of the membrane is defined by  $U_{\text{tot}} = \frac{V}{2} \sigma \cdot \epsilon$ , where  $V$  is the total volume of the TBG drum, from which the restoring force is further obtained by  $F_{\text{res}} = -\frac{1}{D} \cdot \frac{\partial U_{\text{tot}}}{\partial z}$ . Together with the electrostatic pressure  $F_{\text{el}}$  introduced above, the dynamical equation for  $z$  can be constructed by:

$$\frac{d^2 z}{dt^2} = \frac{F_{\text{el}}}{VDm_{\text{eff}}} - \frac{E}{4D^2 m_{\text{eff}}} \left( 2\epsilon_0 z + \frac{z^3}{2} + \tau_o \left( \epsilon_0 + \frac{3}{4} z^2 \right) \frac{dz}{dt} \right) \quad (3)$$

where  $m_{\text{eff}}$  is the effective mass density account for the mode profile of fundamental resonance in a rigidly clamped circular drum<sup>54</sup>,  $\tau_o = \eta/E$  is the viscoelastic relaxation time. The corresponding resonant frequency is given by Eq. (1) in the main text, which is calculated by the output parameters from the numerical solution of the above dynamical equation. Here  $\epsilon_0$  and  $\eta$  are the only two free parameters to fit the experimental frequency loops.

The effect of capacitive softening induced by  $F_{\text{el}}$ <sup>46</sup> on the model is further included by replacing  $F_{\text{el}}(1 + \frac{2D}{d}z)$  in Eq. (3). Accordingly, the resonant frequency is expressed as:

$$f_r = \frac{1}{2\pi} \sqrt{\frac{E}{4m_{\text{eff}}D^2} (k_0 + k_s - k_c)} \quad (4)$$

with the capacitive softening term  $k_c = \frac{8F_{\text{el}}D^2}{EVd}$ . It will reduce to the usual expression for capacitive softening if  $k_s = 0$ , that is, no viscosity.

### Molecular dynamics simulations

MD simulations are performed using the LAMMPS package. The TBG system consists of a rectangular AB-stacked bilayer graphene substrate and a hexagonal AB-stacked bilayer graphene flake. We set the twist angle between the substrate and the flake to 11.64°, i.e., the twist angle of bilayer graphene  $\theta_{\text{TBG}} \sim 11.64^\circ$ , which is close to the experiment. Uniaxial-strain of 0%, 0.5%, 1% is applied to the substrate by changing the coordinates of the carbon atoms to study the effect of heterostrain on the TBG system. The intralayer C-C interactions of graphene are described by the reactive empirical bond order potential, while the interlayer interaction described by the Kolmogorov-Crespi potential<sup>57,58</sup>. To investigate the stable state of the TBG system, we first relax the system out-of-plane while keeping the time-dependent size fixed to maintain the heterostrain. The system is relaxed with an NVT ensemble for 50 ps at a constant temperature of 0.1 K. A load of 2 GPa is then applied to the top layer of the flake to ensure stable contact. The bottom layer of the substrate is fixed and the flake moves along the  $x$ -direction with a driving speed of 10 m s<sup>-1</sup> provided by the top layer of the flake to mimic the interlayer sliding of TBG. The sliding process is simulated at a temperature of 0.1 K.

### Reporting summary

Further information on research design is available in the Nature Portfolio Reporting Summary linked to this article.

### Data availability

The data that support the findings of this study are openly available on Zenodo at <https://doi.org/10.5281/zenodo.15098766>. Additional data are available from the corresponding author upon reasonable request.

### References

1. Lakes, R. S. *Viscoelastic Materials* (Cambridge University Press, Cambridge, 2009).
2. Aklonis, J. J. & MacKnight, W. J. *Introduction to Polymer Viscoelasticity*, 3rd ed. (Wiley-Interscience, Hoboken, N.J., 2005).
3. Chaudhuri, O., Cooper-White, J., Janmey, P. A., Mooney, D. J. & Shenoy, V. B. Effects of extracellular matrix viscoelasticity on cellular behaviour. *Nature* **584**, 535 (2020).
4. Li, X. & Gong, J. P. Design principles for strong and tough hydrogels. *Nat. Rev. Mater.* **9**, 380 (2024).
5. Suhr, J., Koratkar, N., Koblinski, P. & Ajayan, P. Viscoelasticity in carbon nanotube composites. *Nat. Mater.* **4**, 134 (2005).
6. Bunch, J. S. et al. Electromechanical resonators from graphene sheets. *Science* **315**, 490 (2007).
7. Chen, C. et al. Graphene mechanical oscillators with tunable frequency. *Nat. Nanotechnol.* **8**, 923 (2013).
8. Bachtold, A., Moser, J. & Dykman, M. I. Mesoscopic physics of nanomechanical systems. *Rev. Mod. Phys.* **94**, 045005 (2022).
9. Xu, B. et al. Nanomechanical resonators: Toward atomic scale. *ACS Nano* **16**, 15545 (2022).
10. Steeneken, P. G., Dolleman, R. J., Davidovikj, D., Alijani, F. & van der Zant, H. S. J. Dynamics of 2D material membranes. *2D Mater.* **8**, 042001 (2021).
11. Ferrari, P. F., Kim, S. & van der Zande, A. M. Nanoelectromechanical systems from two-dimensional materials. *Appl. Phys. Rev.* **10**, 031302 (2023).
12. Engelsens, N. J., Beccari, A. & Kippenberg, T. J. Ultrahigh-quality-factor micro- and nanomechanical resonators using dissipation dilution. *Nat. Nanotechnol.* **19**, 725 (2024).
13. Bistritzer, R. & MacDonald, A. H. Moiré bands in twisted double-layer graphene. *Proc. Natl. Acad. Sci. USA* **108**, 12233 (2011).
14. Yankowitz, M. Unravelling the magic of twisted trilayer graphene. *Nat. Mater.* **22**, 286 (2023).
15. Cao, Y. et al. Unconventional superconductivity in magic-angle graphene superlattices. *Nature* **556**, 43 (2018).
16. Yankowitz, M. et al. Tuning superconductivity in twisted bilayer graphene. *Science* **363**, 1059 (2019).
17. Lu, X. et al. Superconductors, orbital magnets and correlated states in magic-angle bilayer graphene. *Nature* **574**, 653 (2019).
18. Sharpe, A. L. et al. Emergent ferromagnetism near three-quarters filling in twisted bilayer graphene. *Science* **365**, 605 (2019).
19. Seyler, K. L. et al. Signatures of moiré-trapped valley excitons in MoSe<sub>2</sub>/WSe<sub>2</sub> heterobilayers. *Nature* **567**, 66 (2019).
20. Tran, K. et al. Evidence for moiré excitons in van der Waals heterostructures. *Nature* **567**, 71 (2019).
21. Jin, C. et al. Observation of moiré excitons in WSe<sub>2</sub>/WS<sub>2</sub> heterostructure superlattices. *Nature* **567**, 76 (2019).
22. Wang, L. et al. Correlated electronic phases in twisted bilayer transition metal dichalcogenides. *Nat. Mater.* **19**, 861 (2020).
23. Woods, C. R. et al. Commensurate-incommensurate transition in graphene on hexagonal boron nitride. *Nat. Phys.* **10**, 451 (2014).
24. van Wijk, M. M., Schuring, A., Katsnelson, M. I. & Fasolino, A. Relaxation of moiré patterns for slightly misaligned identical lattices: Graphene on graphite. *2D Mater.* **2**, 034010 (2015).
25. Zhang, S. et al. Domino-like stacking order switching in twisted monolayer-multilayer graphene. *Nat. Mater.* **21**, 621 (2022).
26. Wang, J., Khosravi, A., Vanossi, A. & Tosatti, E. Colloquium: Sliding and pinning in structurally lubric 2D material interfaces. *Rev. Mod. Phys.* **96**, 011002 (2024).

27. Ahn, S. J. et al. Dirac electrons in a dodecagonal graphene quasi-crystal. *Science* **361**, 782 (2018).
28. Hod, O., Meyer, E., Zheng, Q. & Urbakh, M. Structural superlubricity and ultralow friction across the length scales. *Nature* **563**, 485 (2018).
29. Dienwiebel, M. et al. Superlubricity of graphite. *Phys. Rev. Lett.* **92**, 126101 (2004).
30. Han, E. et al. Ultrasoft slip-mediated bending in few-layer graphene. *Nat. Mater.* **19**, 305 (2020).
31. Liao, M. et al. Ultra-low friction and edge-pinning effect in large-lattice-mismatch van der Waals heterostructures. *Nat. Mater.* **21**, 47 (2022).
32. Reijhon, M. et al. Relation between interfacial shear and friction force in 2D materials. *Nat. Nanotechnol.* **17**, 1280 (2022).
33. Banerjee, A. et al. Superfluid stiffness of twisted trilayer graphene superconductors. *Nature* **638**, 93 (2025).
34. Tanaka, M. et al. Superfluid stiffness of magic-angle twisted bilayer graphene. *Nature* **638**, 99 (2025).
35. Zhang, X. et al. Dynamically-enhanced strain in atomically thin resonators. *Nat. Commun.* **11**, 5526 (2020).
36. Lifshitz, R. & Cross, M. C. Nonlinear dynamics of nanomechanical and micromechanical resonators, in *Reviews of Nonlinear Dynamics and Complexity* (John Wiley & Sons, Ltd, 2008) Chap. 1, pp. 1–52.
37. Ying, Y. et al. Sliding nanomechanical resonators. *Nat. Commun.* **13**, 6392 (2022).
38. Wang, G. et al. Measuring interlayer shear stress in bilayer graphene. *Phys. Rev. Lett.* **119**, 036101 (2017).
39. Sun, Y. et al. Determining the interlayer shearing in twisted bilayer MoS<sub>2</sub> by nanoindentation. *Nat. Commun.* **13**, 3898 (2022).
40. Barton, R. A. et al. High, size-dependent quality factor in an array of graphene mechanical resonators. *Nano Lett.* **11**, 1232 (2011).
41. Zhang, S. et al. Dual-scale stick-slip friction on graphene/hBN moiré superlattice structure. *Phys. Rev. Lett.* **128**, 226101 (2022).
42. Socoliuc, A., Bennewitz, R., Gnecco, E. & Meyer, E. Transition from stick-slip to continuous sliding in atomic friction: Entering a new regime of ultralow friction. *Phys. Rev. Lett.* **92**, 134301 (2004).
43. Steele, G. A. et al. Strong coupling between single-electron tunneling and nanomechanical motion. *Science* **325**, 1103 (2009).
44. Lassagne, B., Tarakanov, Y., Kinaret, J., Garcia-Sanchez, D. & Bachtold, A. Coupling mechanics to charge transport in carbon nanotube mechanical resonators. *Science* **325**, 1107 (2009).
45. Song, X. et al. Stamp transferred suspended graphene mechanical resonators for radio frequency electrical readout. *Nano Lett.* **12**, 198 (2012).
46. Weber, P., Güttinger, J., Tsioutsios, I., Chang, D. E. & Bachtold, A. Coupling graphene mechanical resonators to superconducting microwave cavities. *Nano Lett.* **14**, 2854 (2014).
47. Wopereis, M. P. F. et al. Tuning dissipation dilution in 2D material resonators by MEMS-induced tension. *J. Appl. Phys.* **136**, 014302 (2024).
48. Gibertini, M., Koperski, M., Morpurgo, A. F. & Novoselov, K. S. Magnetic 2D materials and heterostructures. *Nat. Nanotechnol.* **14**, 408 (2019).
49. Huang, X. et al. Microscale schottky superlubric generator with high direct-current density and ultralong life. *Nat. Commun.* **12**, 2268 (2021).
50. Koren, E. et al. Coherent commensurate electronic states at the interface between misoriented graphene layers. *Nat. Nanotechnol.* **11**, 752 (2016).
51. Huang, Y. et al. Raman spectral band oscillations in large graphene bubbles. *Phys. Rev. Lett.* **120**, 186104 (2018).
52. Ma, X. et al. Capillary-force-assisted clean-stamp transfer of two-dimensional materials. *Nano Lett.* **17**, 6961 (2017).
53. Hou, Y. et al. Preparation of twisted bilayer graphene via the wetting transfer method. *ACS Appl. Mater. Interfaces* **12**, 40958 (2020).
54. Davidovikj, D. et al. Visualizing the motion of graphene nanodrums. *Nano Lett.* **16**, 2768 (2016).
55. Pandey, V. et al. Probing interlayer interactions and commensurate–incommensurate transition in twisted bilayer graphene through Raman spectroscopy. *ACS Nano* **18**, 4756 (2024).
56. Güttinger, J. et al. Energy-dependent path of dissipation in nanomechanical resonators. *Nat. Nanotechnol.* **12**, 631 (2017).
57. Brenner, D. W. et al. A second-generation reactive empirical bond order (rebo) potential energy expression for hydrocarbons. *J. Phys.: Condens. Matter* **14**, 783 (2002).
58. Kolmogorov, A. N. & Crespi, V. H. Registry-dependent interlayer potential for graphitic systems. *Phys. Rev. B* **71**, 235415 (2005).

## Acknowledgements

We thank F. N. Chen and H. Lu for their help in the exploration of ring-down measurements. This work is supported by the National Natural Science Foundation of China (Grant No. 12174381). X.Z. acknowledges support from the CAS BR Scholar project, Young Science and Technology Talent Promotion Program funded by Institute of Semiconductors, Beijing Natural Science Foundation (Grant No. Z2200005), and CAS Project for Young Scientists in Basic Research (Grant No. YSBR-030). P.T. acknowledges support from the National Natural Science Foundation of China (Grant Nos. 12127807, 12393832). J.M. acknowledges support from the National Natural Science Foundation of China (Grant Nos. 62150710547, 62074107). A.S. and T.M. acknowledges support from the National Natural Science Foundation of China (Grant Nos. 52225502, 52305200, 52363033). Z.Z. and X.S. acknowledges support from the National Natural Science Foundation of China (Grant Nos. 12274397, 12274401), the National Key Research and Development Program of China (Grant No. 2022YFA1405900). G.D. acknowledges support from the National Natural Science Foundation of China (Grant No. 12074058), the National Key Research and Development Program of China (Grant No. 2022YFA1405900).

## Author contributions

Q.Z., G.S., and A.S. contributed equally to this work. X.Z. designed the research project and built the experimental setup. Q.Z., G.S., X.M. and X.Z. fabricated the samples. X.Z., Q.Z., and G.S. carried out optomechanical, the ring-down, and micro-Raman spectroscopy measurements. X.Z., Q.Z., P.T., and G.S. analysed the data with input from J.M., Y.Y., Z.Z., and X.S. A.S., Z.X., and T.M. performed the molecular dynamic simulations. X.Z. and J.M. wrote the manuscript with input from Q.Z., G.S., A.S., X.M., Y.Y., G.D., and P.T. P.T. and X.Z. supervised the project.

## Competing interests

The authors declare no competing interests.

## Additional information

**Supplementary information** The online version contains supplementary material available at <https://doi.org/10.1038/s41467-025-58981-2>.

**Correspondence** and requests for materials should be addressed to Joel Moser, Ping-Heng Tan or Xin Zhang.

**Peer review information** *Nature Communications* thanks the anonymous, reviewer(s) for their contribution to the peer review of this work. A peer review file is available.

**Reprints and permissions information** is available at <http://www.nature.com/reprints>

**Publisher's note** Springer Nature remains neutral with regard to jurisdictional claims in published maps and institutional affiliations.

**Open Access** This article is licensed under a Creative Commons Attribution-NonCommercial-NoDerivatives 4.0 International License, which permits any non-commercial use, sharing, distribution and reproduction in any medium or format, as long as you give appropriate credit to the original author(s) and the source, provide a link to the Creative Commons licence, and indicate if you modified the licensed material. You do not have permission under this licence to share adapted material derived from this article or parts of it. The images or other third party material in this article are included in the article's Creative Commons licence, unless indicated otherwise in a credit line to the material. If material is not included in the article's Creative Commons licence and your intended use is not permitted by statutory regulation or exceeds the permitted use, you will need to obtain permission directly from the copyright holder. To view a copy of this licence, visit <http://creativecommons.org/licenses/by-nc-nd/4.0/>.

© The Author(s) 2025